Available online at www.sciencedirect.com
ScienceDirect
Cement & Concrete Composites 29 (2007) 117–123
Cement & Concrete Composites
www.elsevier.com/locate/cemconcomp

Effect of supplementary cementitious materials on shrinkage and crack development in concrete

Yilmaz Akkaya [a,*], Chengsheng Ouyang [b], Surendra P. Shah [c]

[a] Istanbul Technical University, Civil Engineering Faculty, Maslak, Istanbul 34469, Turkey
[b] Iowa D.O.T., Office of Materials, 800 Lincoln Way, Ames, IA 50010, United States
[c] Center for ACBM, Northwestern University, 2145 Sheridan Road, Evanston, IL 60208, United States

Received 23 October 2005; received in revised form 3 October 2006; accepted 4 October 2006
Available online 21 November 2006

Abstract

The autogenous and drying shrinkage of Portland cement concrete, and binary and ternary binder concretes, were measured and compared. The binary and ternary binder concretes were formed by replacing part of the cement with fly ash, very fine fly ash and/or silica fume. Restrained shrinkage test was also performed to evaluate the effect of binder type on early age cracking. After the cracking of the restrained ring samples, crack widths were measured and compared with the results of an *R*-curve based model, which takes post-peak elastic and creep strains into account.

The incorporation of fly ash and very fine fly ash decreased the autogenous shrinkage strain but increased the drying shrinkage strain. Since the total shrinkage strains of both the ternary and the binary concrete mixtures were similar, the strength development became an important factor in the cracking. The lower strength of the concrete with ternary binders led to earlier cracking compared to the binary binder concrete. Portland cement concrete cracked the earliest and had the greatest crack width. Measured crack widths were in accordance with the crack widths calculated with the *R*-curve model.

Keywords: Autogenous shrinkage; Restrained shrinkage; Cracking; Early age; *R*-curve

1. Introduction

Early age cracking is a major concern for the durability of concrete structures. Autogenous shrinkage, together with drying shrinkage, may result in cracking under restrained conditions. The total shrinkage stress that eventually leads to cracking of the concrete is also accompanied by creep. The crack size depends on the extent of the elastic and creep stresses, as well as the mechanical strength of the concrete [1–7].

Calculating the fracture parameters and modeling the development of early age crack width can be a useful tool in design of concrete mixtures. This study investigates the effect of binary and ternary binders on the early age cracking of concrete. Fly ash, very fine fly ash and silica fume were used in the binder phase and their effects on the shrinkage, creep and mechanical properties were determined at early ages. The resulting crack widths of restrained shrinkage samples were measured and compared with the crack widths calculated by an *R*-curve approach.

2. Materials design and experimental studies

Type I Portland cement, Class F fly ash, Class F very fine fly ash and silica fume powder were used in the binder phase of the concrete. The total cementitious material of the concrete mixes was 403–438 kg/m^3. The specific gravity of the silica fume was 2.2 g/cm^3 and average particle size was 0.1 μm. The average particle size of the Class F (ASTM C618) very fine fly ash was 3 μm and had a specific gravity of 2.55 g/cm^3. Over 90% of the very fine fly ash

* Corresponding author. Tel.: +90 212 2853769; fax: +90 212 2856587.
E-mail address: akkayayil1@itu.edu.tr (Y. Akkaya).

0958-9465/$ - see front matter © 2006 Elsevier Ltd. All rights reserved.
doi:10.1016/j.cemconcomp.2006.10.003

Table 1
Chemical composition of very fine fly ash (VFA), fly ash (FA) and Portland cement (PC) (by % of weight)

	SiO_2	Al_2O_3	Fe_2O_3	CaO	MgO	K_2O	SO_3
VFA	48.43	26.23	3.74	14.08	2.5	0.6–1.1	0.9
FA	57.64	19.23	4.45	12.01	2.43	0.83	0.37
PC	20.7	4.7	2.6	65.7	2.2	–	2.5

particles passed from a 7 μm sieve. The chemical composition of the very fine fly ash is given in Table 1. The reactivity of very fine fly ash is higher than regular fly ash due to its increased specific surface area and the autogenous shrinkage of the concrete made with very fine fly ash has a lower rate of increase compared to that of concrete made with silica fume [8,9]. Specific gravity of the Class F fly ash used in this study was 2.3 g/cm^3. The chemical composition of the fly ash is given in Table 1.

A melamine-based superplasticizer was used in order to ensure the workability of the concrete. The superplasticizer used was 0.8–1.2% by the weight of cementitious materials in the mixes and provided a slump of 11–13 cm for the fresh concrete. The water-to-cementitious materials ratios of the mixes were in the range of 0.35–0.38 (by weight).

The mix designs and codes of the concretes used in the experiments are given in Table 2. Two binary and two ternary mix designs were investigated and compared with the Portland cement concrete. Fly ash, very fine fly ash and silica fume were used as replacements in the binder phase for an equivalent volume of cement. The contents of fly ash, very fine fly ash and silica fume were determined depending on the practical usage limits. The total aggregate volume in the concrete was 67%.

Free and restrained shrinkage tests were performed in order to evaluate and compare the autogenous and drying shrinkage properties and shrinkage cracking of the binary and ternary mixes. The development of dynamic modulus of elasticity was measured by resonance frequency until the cracking-day. Compression and three-point bending tests were performed on the concrete at fourteen days of age in order to compare the mechanical performances.

Free drying shrinkage tests were performed on concrete specimens of $100 \times 100 \times 400$ mm. Three specimens were used for each type of concrete. Specimens were evenly dried from two opposite 100×400 mm surfaces, and sealed on the other surfaces, in order to keep the same volume-to-surface ratio as the ring specimens. For the autogenous shrinkage samples, stainless steel gage studs were embedded on both sides of the fresh concrete, providing a gage length of 350 mm. Two detachable mechanical gages were used for measuring shrinkage from the time of initial setting up to 24 h. After 24 h, shrinkage measurements were determined according to ASTM C 341. Immediately after demolding the specimens for the autogenous shrinkage measurements, specimens were sealed with adhesive aluminum sheets completely and kept under controlled temperature (30 °C) and humidity (40%) chamber.

In order to quantify the effect of restrained shrinkage on the cracking, ring tests were used [2–6]. Cracking of the concrete restrained by a ring would depend on the curing conditions, material composition and the thickness of the surrounding concrete and the steel ring. Specimens with a 5 cm thickness, 30.5 cm inner diameter and 14.9 cm height were cast around a rigid steel ring. The exterior mold was removed 24 h after casting. Three specimens were cast for each type of concrete. Two strain gages were mounted on the inside perimeter of the steel ring in order to measure the development of confining strains imposed by the concrete, cast around the steel ring. The day at which the cracking starts was determined by the sharp drop in the confining strain–time curve. After the cracking of the concrete, the development of the crack widths was measured by a microscope.

Specimens for the compression tests were cured in a controlled temperature (30 °C) and humidity (40%) chamber until the age of testing. The compressive strength of cylindrical concrete specimens of 100×200 mm was determined according to the ASTM C 39 under stroke control at 14th day of age and was calculated as the average of three specimens with consistent results.

Three-point bend tests were performed to assess the flexural performance of concrete. Beams of 50 mm × 100 mm × 450 mm were cast, demolded after 24 h and cured in controlled temperature (30 °C) and humidity (40%) chamber for 14 days. Three samples were used for each concrete type. A notch was cut to one-third the depth of the beam, and beams were tested over a 400 mm span. An extensometer was mounted across the notch to measure the crack mouth opening displacement and provide feedback to control loading. Two LVDTs were yoke-mounted on either side of the specimen to measure deflection. The flexural strength was calculated based on the maximum flexural stress. Modulus of elasticity was determined based on the

Table 2
Mixture proportions for 1 m^3 of concrete

Mixture code	Binder phase	Cement (kg)	Silica fume (kg)	Very fine fly ash (kg)	Fly ash (kg)	Water (kg)	Fine agg. (kg)	Coarse agg. (kg)
C	100% PC	438	0	0	0	155	778	966
CU	90%PC + 10%VFA	394	0	35	0	155	778	967
CF	80%PC + 20%FA	350	0	0	64	155	777	965
CFU	70%PC + 20%FA + 10%VFA	307	0	35	64	155	779	967
CSF	72%PC + 20%FA + 8%SF	315	24	0	64	155	777	965

initial compliance calculated from the load–CMOD curve [10]. The development of the elasticity modulus was followed by resonance frequency method. The dynamic modulus of elasticity calculated from the resonance frequency usually gives a higher value compared to that of its static value. However, the preceding values of the static elasticity modulus can be determined based on the development of the dynamic modulus of elasticity [11].

3. Test results

The total, autogenous and drying shrinkage of all the concrete samples are given in Fig. 1. Concrete with Portland cement as the only binder exhibited the highest autogenous shrinkage, whereas concrete with ternary binders exhibited the lowest autogenous shrinkage. The autogenous shrinkage of the concrete with 10% very fine fly ash replacement (CU) was closer to the Portland cement concrete, and the autogenous shrinkage of the concrete with 20% fly ash replacement (CF) was closer to the concrete with ternary binders. The drying shrinkage is calculated as the difference between the total shrinkage and the autogenous shrinkage. As the autogenous shrinkage of the concrete decrease, the drying shrinkage increases due to the differences in pore structure connectivity [12]. There is no significant difference in the total shrinkage of the concrete.

The effect of binary and ternary binders on the mechanical properties, at the 14th day after casting, is presented in

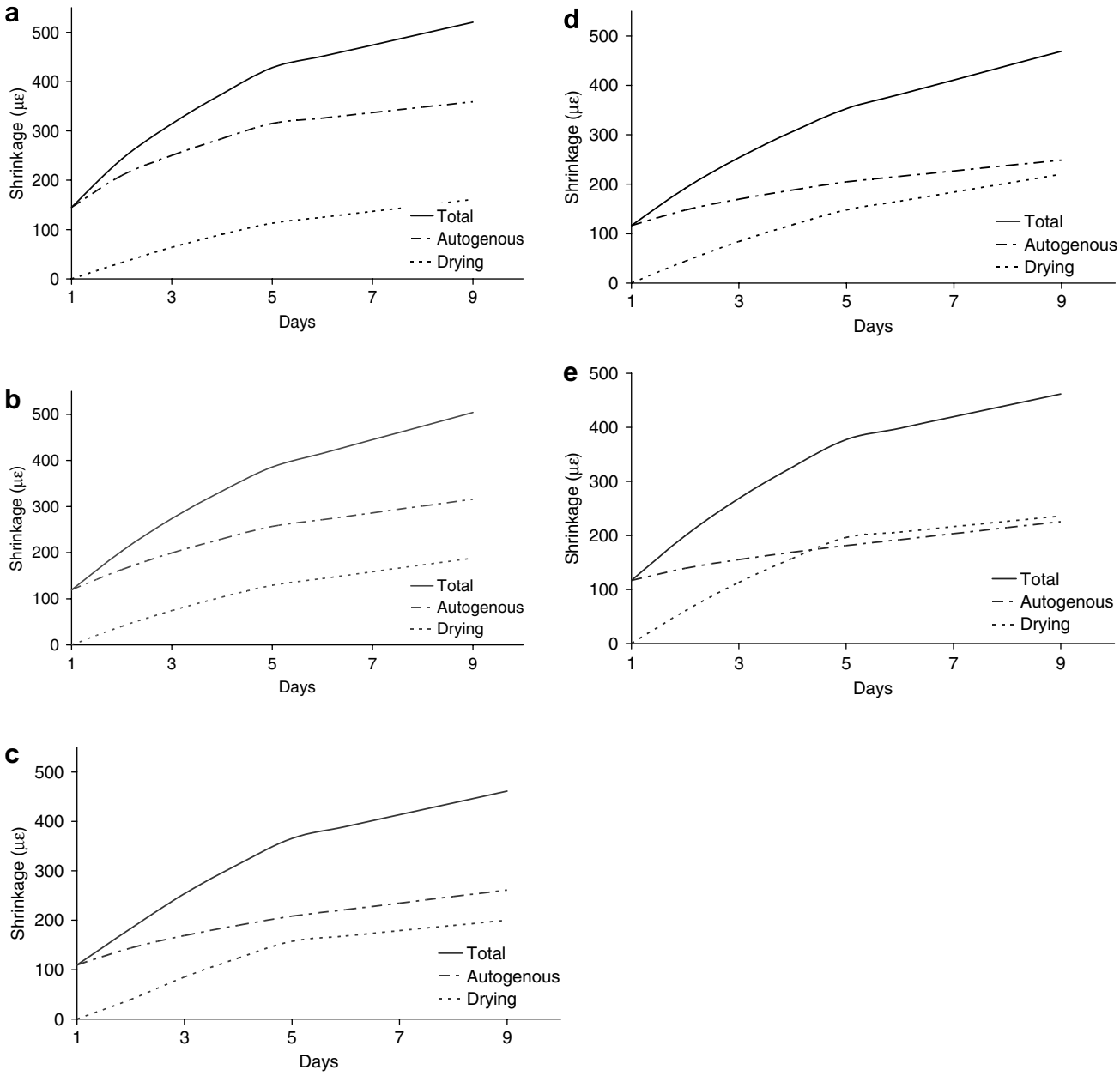

Fig. 1. Total, autogenous and drying shrinkage strains of the mixes (a) C, (b) CU, (c) CF, (d) CFU and (e) CSF.

Table 3
Mechanical properties and modulus of elasticity of the concrete

	Flexural strength (MPa)	Compressive strength (MPa)	Modulus of elasticity (MPa)
C	4.67	50.4	29.0
CU	4.58	48.4	27.9
CF	4.31	44.2	25.3
CFU	4.01	40.3	25.7
CSF	4.14	41.2	24.1

Table 3. The highest decrease in the compressive and flexural strength was seen with the ternary binders. Compared to the concrete with Portland cement as the only binder, the decreases in the compressive and flexural strengths of the concrete with fly ash and very fine fly ash (CFU) were 20% and 14%, respectively. The decreases in the compressive and flexural strengths in the concrete with fly ash and silica fume (CSF) were 19% and 11%, respectively. The decreases in the compressive and flexural strengths of the concrete with binary binders (CU and CF) were less than 10% compared to the Portland cement concrete.

The development of the dynamic modulus of elasticity of the concrete is given in Fig. 2. Concrete with Portland cement as the only binder exhibited the highest dynamic modulus of elasticity, where the ternary binder concrete had the lowest. The lower amount of cement content and the greater amount of pozzolans in the ternary mixes are the reasons for lower strength of this type of concrete.

The development of the confining strains, measured from the restrained shrinkage ring test, is given in Fig. 3. The discontinuity and sharp drop in the strains indicate the release of strains due to cracking of concrete. It can be seen that plain cement concrete cracked earlier than the binary and ternary binder concrete. The cracking-days of the concrete are 6.1, 8.5, 8.2, 7.5 and 7.2 for C, CU, CF, CFU and CSF, respectively. The use of fly ash and very fine fly ash delayed the cracking. Although the elasticity modulus of the ternary binder concrete was lower, they cracked earlier than the binary binder concrete due to their reduced mechanical strengths.

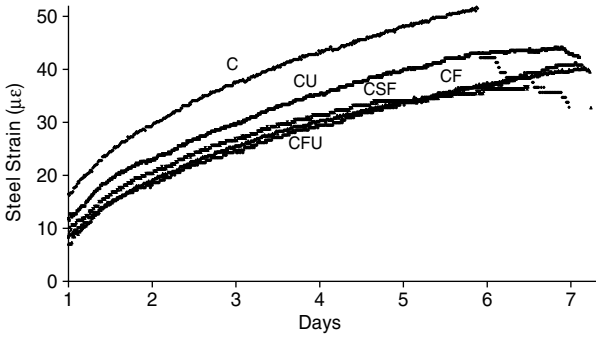

Fig. 3. The measured strain in the steel ring.

Although the autogenous shrinkage strains were reduced with the use of fly ash and very fine fly ash, the drying shrinkage strains were higher with the ternary mixes. This resulted in similar total shrinkage strains. The total shrinkage strains of the concrete at seventh day were, 474, 444, 413, 419, 410 με for C, CU, CF, CSF and CFU, respectively. Since the total shrinkage strains of the binary and ternary concrete were similar, the strength development became an important factor in the cracking. The lower strength of the concrete with ternary binders led to earlier cracking. The strength of binary binder concrete did not decrease as much as ternary binder concrete and thus, the binary binder concrete cracked the latest.

The development of the creep in the concrete mixes can be obtained by using the strain measured in the restraining steel ring and the shrinkage of the free specimen [6,13,14]. The development of creep coefficients is presented in Fig. 4. The creep coefficient increased slightly with the addition of supplemental cementitious materials. It can be seen that creep is a major factor in the cracking of early age restraint concrete, as the ratio of creep to shrinkage strain reached to a value of 0.4 in 3 days and 0.47 in 7 days.

The crack widths measured after the cracking of restrained shrinkage specimens, are presented in Fig. 5. Portland cement concrete had the greatest crack width, due to its earlier start. The binary mixes exhibited the lowest value of crack widths.

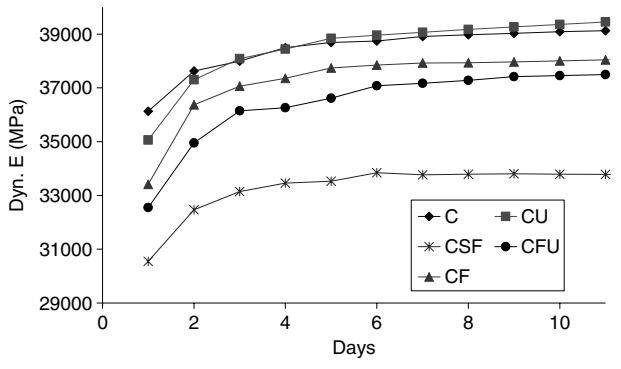

Fig. 2. Development of dynamic modulus of elasticity of the concrete.

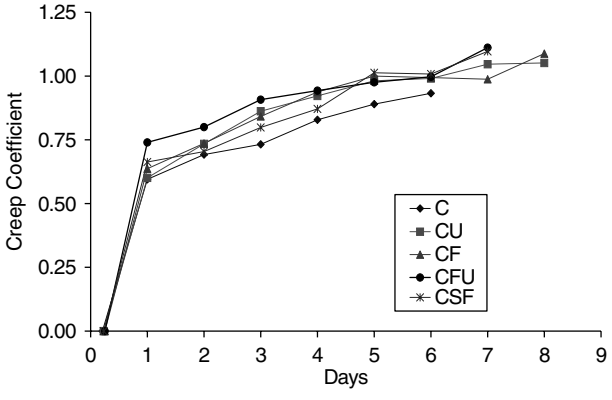

Fig. 4. Development of the creep coefficient.

4. Restrained shrinkage crack width model

This section attempts to model the development of crack widths, based on an *R*-curve model. For this reason, the flexural test data is used to evaluate the post-peak stress–crack width relationship under tension.

The development of the crack width in a restrained shrinkage ring specimen can be modeled using the measured quantities of free shrinkage strain and creep, and the cohesive tensile crack width–stress relationship. The cohesive tensile behavior can be used to describe stress transfer across the crack by crack-arresting mechanisms, such as aggregate interlock or friction [15]. This cohesive tensile behavior of the concrete can be evaluated based on a three-point bend beam test. Hence, after the crack opening, the measured shrinkage strain of the free sample ε_{sh} at time t, can be expressed as follows:

$$\varepsilon_{sh}(t) = \frac{w(t)}{2\pi r} + \frac{\sigma_e[w(t)]}{E_c(t)}(1 + \phi_{cr}(t)) + \varepsilon_u \quad (1)$$

where, $w(t)$ is the crack opening at time t, r is the radius of the mid-section of the concrete ring, $\sigma_e[w(t)]$ is the elastic stress (residual stress) corresponding to a crack width at time t, $E_c(t)$ is the elastic modulus of concrete, $\phi_{cr}(t)$ is the creep coefficient and ε_u is the elastic unloading strain. It was assumed that even after cracking, the creep coefficient for uncracked part of concrete follows the same tendency as before cracking. The creep coefficients shown in Fig. 5 were fitted by power curves and used in the following theoretical prediction.

The elastic unloading strain ε_u can be calculated by σ_{max}, the maximum stress of the restraint concrete at the time of cracking, and E_c, the modulus of elasticity of concrete at the time of cracking,

$$\varepsilon_u = \frac{\sigma_{max} - \sigma_e(w)}{E_c} \quad (2)$$

The tensile cohesive stress transfer $\sigma_e(w)$ depends on the crack width, w, and can be measured from the tensile test. However, since direct tensile measurement is difficult to perform, this tensile cohesive stress was derived from flexural stress vs. crack mouth opening displacement (CMOD) measurements based on fracture mechanics approach [16]. As described in Fig. 6, the approach first calculates the *R*-crack length relationship from the flexural stress–CMOD curve. The material fracture parameters can be calculated by this flexural *R*-curve and these parameters can be used for generating the *R*-crack length relationship for tension specimen of the same material. Then the tensile stress–CMOD relationship can be calculated based on the tensile *R*-curve. The procedure is outlined below.

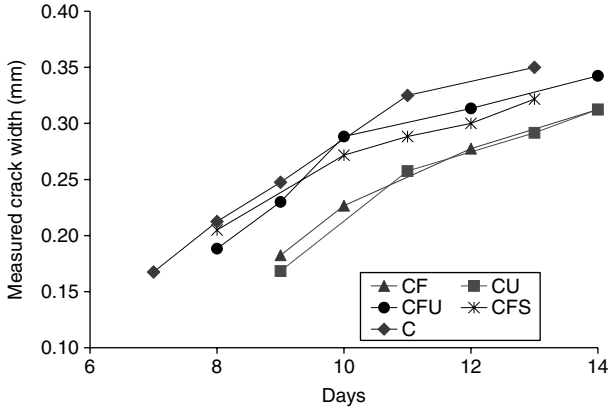

Fig. 5. Measured crack widths of the specimens.

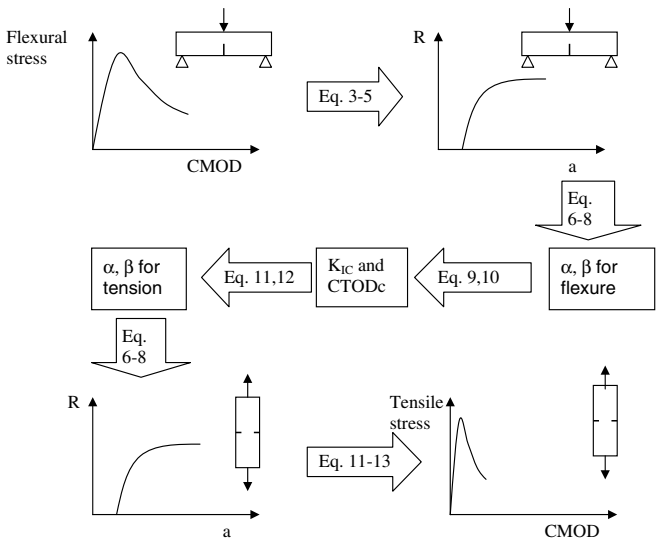

Fig. 6. Summary of the model.

First, for each set of measured values of applied stress, σ, and crack mouth opening displacement, CMOD, from a three-point bending beam, the corresponding value of the crack length, a, can be calculated by the relationship given below [15,17]:

$$\mathrm{CMOD} = \frac{4\sigma a}{E}\left[0.76 - 2.28(a/b) + 3.87(a/b)^2 - 2.04(a/b)^3 + \frac{0.66}{(1-a/b)^2}\right] \quad (3)$$

Here, b is the depth of the beam. Then, the stress intensity factor, K_I, and the strain energy release rate, G, can be determined by

$$K_I = \sigma\sqrt{\pi a}\left\{\frac{1.99 - (a/b)(1-a/b)[2.15 - 3.93(a/b) + 2.7(a/b)^2]}{\sqrt{\pi}(1+2(a/b))(1-a/b)^{3/2}}\right\} \quad (4)$$

and

$$G = \frac{K_I^2}{E} \quad (5)$$

Crack propagation occurs when the strain energy release rate is equal to the fracture resistance, R. By using this energy balance condition, the *R*-curve for a flexural speci-

men can be experimentally obtained. On the other hand, a theoretical R-curve can also be expressed as a function of crack length, a, and two parameters α and β.

$$R = \beta\psi(a - a_0)^{d_2} \tag{6}$$

$$\psi = 1 - \frac{d_2\alpha - \alpha + 1}{d_1\alpha - \alpha + 1}\left(\frac{\alpha a_0 - a_0}{a - a_0}\right)^{d_2 - d_1} \tag{7}$$

$$d_{1,2} = \frac{1}{2} + \frac{\alpha - 1}{\alpha} \pm \left[\frac{1}{4} + \frac{\alpha - 1}{\alpha} - \left(\frac{\alpha - 1}{\alpha}\right)^2\right]^{1/2} \tag{8}$$

where a_0 is the initial notch length, and assumed to be 2 mm in this study, a reasonable value for the given dimensions of the test specimen. The parameters α and β are dependent on material fracture property and specimen geometry. In order to calculate α and β, two points are selected from the experimentally obtained R-curve and substituted into the Eqs. (6)–(8). Thus, a system of two equations and two unknowns is created and solved. The first point, (a_A, R_A), is taken as the crack length at the peak load, whereas the second point, (a_B, R_B), is taken as the point at which the R-curve changed its curvature due to the increasing effect of the inelastic portion of the fracture energy.

After α and β for the three-point bending beam are determined, the fracture parameters (the critical stress intensity factor, K_{IC}, and the critical crack-tip-opening displacement, $CTOD_c$) can be determined by the following expressions [15]:

$$\alpha = \frac{\pi E^2 f_1^2 \mathrm{CTOD}_c^2}{32 a_0 K_{IC}^2 f_2^2} + \sqrt{\left[\frac{\pi E^2 f_1^2 \mathrm{CTOD}_c^2}{32 a_0 K_{IC}^2 f_2^2}\right] + 1} \tag{9}$$

$$\beta = \frac{K_{IC}^2(d_1\alpha - \alpha - 1)}{E\alpha(d_1 - d_2)(\alpha a_0 - a_0)^{d_2}} \tag{10}$$

For three-point bending beams, $f_1 = 1.123$ and $f_2 = 1.42$ and for uniaxial tension specimens, $f_1 = 1.123$, and $f_2 = 1.454$ [17]. Once K_{IC} and CTODc (material fracture parameters independent of specimen geometry) are calculated, the material response in other loading configurations is determined. α and β for uniaxial tension are calculated from K_{IC} and CTODc, using the appropriate values of f_1 and f_2. The calculated parameters of α, β, K_{IC} and $CTOD_C$ are given in Table 4.

By applying the energy balance $R = G$ for uniaxial tensile specimen, tensile stress and crack extension can be calculated. Then, K_I can be evaluated by

$$K_I = (G \cdot E)^{1/2} = (RE)^{1/2} \tag{11}$$

Here K_I for uniaxial tension is [15],

$$K_I = \sigma\sqrt{\pi a}[1.122 - 0.231(a/b) + 10.55(a/b)^2 - 21.71(a/b)^3 + 30.382(a/b)^4] \tag{12}$$

Hence, stress–crack length (σ–a) relationship is evaluated from Eqs. (11 and 12) by solving for σ. Then, the tensile displacement due to crack extension, w, can be calculated by the following equations:

$$w = \delta - \delta_0$$

$$\delta = PC = \sigma\left(\frac{L}{E} + \int_0^a \frac{2R}{\sigma^2 b}\mathrm{d}a\right) \tag{13}$$

$$\delta_0 = \varepsilon L = \frac{\sigma L}{E} = \frac{PL}{Ebt}$$

where δ is the total displacement, P ($=\sigma bt$) is the total load, C is compliance, L is the specimen length, b is the specimen depth, t is the specimen width, δ_0 is the elastic displacement, E is the elasticity modulus of concrete and t is the thickness of specimen. The cohesive tensile stress–crack width relation obtained by the R-curve method is shown in Fig. 7.

Table 4
Calculated material fracture parameters for the concrete

	α (from flexural test)	β (from flexural test)	K_{IC} (MPa mm$^{1/2}$)	$CTOD_c$ (mm)
C	3.229	0.0173	71.84	0.069
CU	3.045	0.0167	64.53	0.063
CF	2.944	0.0138	53.72	0.056
CFU	2.650	0.0155	50.47	0.049
CSF	2.796	0.0162	53.23	0.057

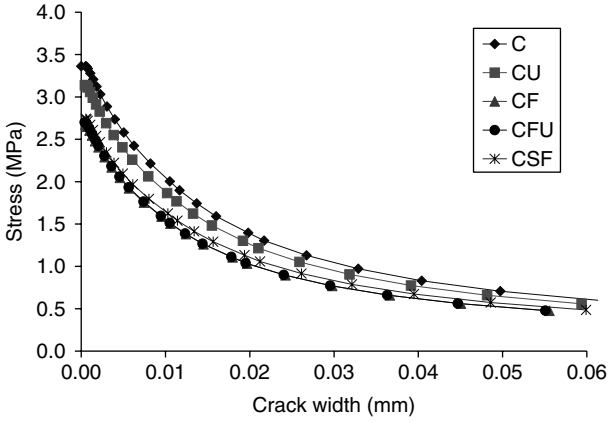

Fig. 7. Cohesive tensile stress–crack width relationship.

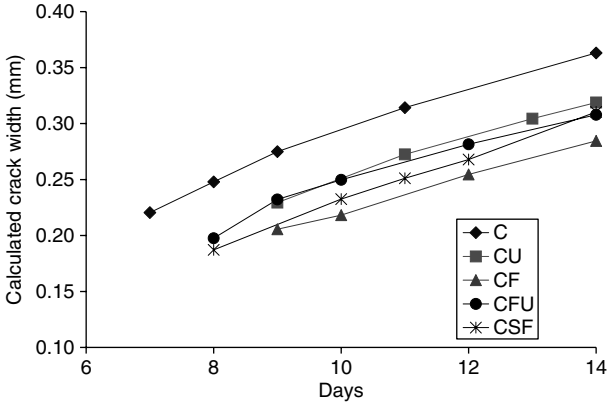

Fig. 8. Calculated crack width–time relationship.

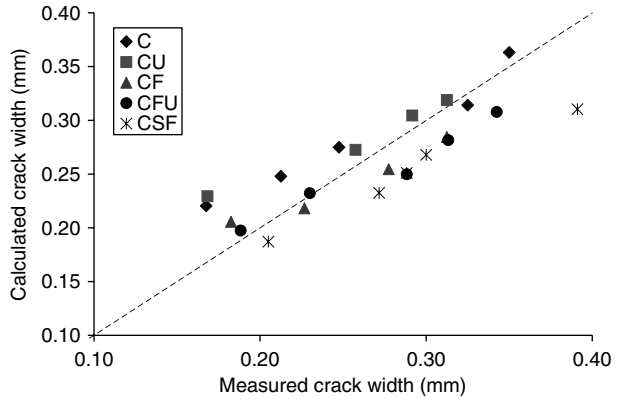

Fig. 9. Calculated vs. measured crack widths.

After the determination of the cohesive stress, $\sigma_e[w(t)]$, for a given crack width, the crack width, w, can be calculated using Eq. (1) based on the measured values of free shrinkage strain and creep. Calculated crack width vs. time relationship is given in Fig. 8. The measured crack width vs. calculated crack width relationship is presented in Fig. 9. It can be seen that calculated and measured crack widths reasonably agree each other and the proposed model can be used to estimate the crack widths.

5. Summary and conclusions

The ternary concrete mixes exhibited lower autogenous shrinkage strains and larger drying shrinkage strains compared to the binary concrete mixes. This resulted in similar total shrinkage strains for both types of concrete, and the strength development became an important factor in the cracking. The lower strength of the concrete with ternary binders led to earlier cracking, although they had lower modulus of elasticity. The strength of binary binder concrete did not decrease as much, and cracked the latest. Portland cement concrete mix cracked the earliest and had the greatest crack width.

An R-curve based model has been proposed to predict cracking response of early age concrete, based on available flexural test results. The R-curve for the flexural test was used for calculating the fracture parameters K_{IC} and CTODc. These parameters were used to generate the corresponding R-curve for uniaxial tension. The tensile stress–displacement relationship was calculated by the obtained R-curve for tension. After the determination of the tensile stress–displacement relationship, the residual elastic stresses after cracking can be estimated. By taking the residual elastic stress and creep into account, the crack width development of the restrained concrete specimens was predicted.

References

[1] Wiegrink K, Marikunte S, Shah SP. Shrinkage cracking of high strength concrete. ACI Mater J 1996;93(5):409–15.
[2] Grzybowski M, Shah SP. Shrinkage cracking of fiber reinforced concrete. ACI Mater J 1990;87(2):138–48.
[3] Weiss WJ, Shah SP. Restrained shrinkage cracking: the role of shrinkage reducing admixtures and specimen geometry. Mater Struct 2002;35:85–91.
[4] Shah S, Karaguler M, Sarigaphuti M. Effects of shrinkage-reducing admixtures on restrained shrinkage of concrete. ACI Mater J 1992;89(3):289–95.
[5] Shah S, Ouyang C, Marikunte S, Yang W, Becq-Giraudon E. A method to predict shrinkage cracking of concrete. ACI Mater J 1998;95(4):339–46.
[6] See HT, Attiogbe EK, Miltenberger MA. Shrinkage cracking characteristics of concrete using ring specimens. ACI Mater J 2003;100(3):239–45.
[7] Igarashi S, Bentur A, Kovler K. Autogenous shrinkage and induced restraining stresses in high-strength concrete. Cement Concrete Res 2000;30:1701–7.
[8] Obla KH, Hill RL, Thomas MDA, Shashiprakash SG, Perebatova O. Properties of concrete containing very-fine fly ash. ACI Mater J 2003;100(5):426–33.
[9] Subramaniam KV, Gromotka R, Shah SP, Obla K, Hill R. The influence of ultra fine fly ash on the early-age mechanical and shrinkage characteristics of concrete. J Mater Civil Eng 2005;17(1):45–53.
[10] RILEM TC89-FMT fracture mechanics of concrete test methods, determination of fracture parameters of plain concrete using three-point bend tests. Mater Struct 1990;23:457–60.
[11] Hossain AB, Weiss WJ. Assessing residual stress development and stress relaxation in restrained concrete ring specimens. Cement Concrete Compos 2004;26(5):531–40.
[12] Akkaya Y, Konsta-Gdoutos M, Shah SP. The pore structure and autogenous shrinkage of high-performance concrete with ternary binders. ACI Special Publication 2004;221:233–48.
[13] Yang E, Yi S, Lee H. Mechanical characteristics of axially restrained concrete specimens at early ages. J Mater Civil Eng 2004;16(1):35–44.
[14] Grasley ZC, Lange DA. Early-age concrete stresses induced by driving shrinkage and thermal dilation. In: Proceedings of the fifth international Ph.D. symposium in civil engineering, Delft, 2004.
[15] Shah SP, Swartz WE, Ouyang C. Fracture mechanics of concrete: applications of fracture mechanics to concrete, rock, and other quasi-brittle materials. New York: John Wiley & Sons; 1995.
[16] Cyr M, Ouyang C, Shah SP. Design of hybrid-fiber reinforcement for shrinkage cracking by crack width predictions. In: Brandt AM, Li VC, Marshall IH, editors. Brittle matrix composites, vol.7. Woodhead Publishing Limited; 2003. p. 243–52.
[17] Tada H, Paris PC, Irwin GR. The stress analysis of cracks handbook. St. Louis: Paris Productions; 1985.